ACS OMEGA

http://pubs.acs.org/journal/acsodf

Article

Molecular-Weight-Dependent Interplay of Brittle-to-Ductile Transition in High-Strain-Rate Cold Spray Deposition of Glassy Polymers

Anuraag Gangineri Padmanaban, Tristan W. Bacha, Jeeva Muthulingam, Francis M. Haas, Joseph F. Stanzione, III, Behrad Koohbor, and Jae-Hwang Lee*

Cite This: *ACS Omega* 2022, 7, 26465−26472

Read Online

ACCESS | Metrics & More | Article Recommendations | Supporting Information

ABSTRACT: Based on the cold spray technique, the solvent-free and solid-state deposition of glassy polymers is envisioned. Adiabatic inelastic deformation mechanisms in the cold spray technique are studied through high-velocity collisions (<1000 m/s) of polystyrene microparticles against stationary target substrates of polystyrene and silicon. During extreme collisions, a brittle-to-ductile transition occurs, leading to either fracture- or shear-dominant inelastic deformation of the colliding microparticles. Due to the nonlinear interplay between the adiabatic shearing and the thermal softening of polystyrene, the plastic shear flow becomes the dominant deformation channel over brittle fragmentation when increasing the rigidity of the target substrate. High molecular weights (>20 kDa) are essential to hinder the evolution of brittle fracture and promote shear-induced heating beyond the glass transition temperature of polystyrene. However, an excessively high molecular weight (∼100 kDa) reduces the adhesion of the microparticles to the substrate due to insufficient wetting of the softened polystyrene. Due to the two competing viscoelastic effects, proper selection of molecular weight becomes critical for the cold spray technique of glassy polymers.

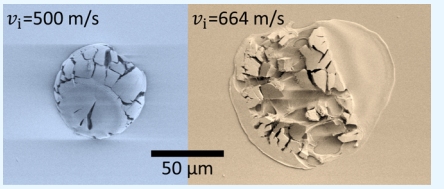

INTRODUCTION

Solid-state coating of materials is feasible by the cold spray (CS) technique, in which solid feedstock powders or microparticles (μPs) are accelerated by a supersonically expanding stream of carrier gasses and are subjected to a head-on collision against a stationary surface at transonic or supersonic velocities.[1] Due to the collision-induced adiabatic deformation, the solid-state consolidation of μPs is possible for coating and additive manufacturing.[2] Although CS has primarily been developed for metal deposition, similar principles can be applied for solventless deposition of polymers.[3,4] Moreover, the anisotropic shear flows within the deforming μPs can lead to the ordering of polymer chains[5] along the surface of a substrate. Thus, the polymer coatings produced by CS may exhibit a higher in-plane strength if the ordering effect is preserved due to the short time scale (<400 ns)[6] of the plastic deformation. In addition to the practical importance of CS, the study of the collision-induced deformation characteristics of μPs will lead to a deeper understanding of the rheological properties of macromolecules under the thermodynamically nonequilibrium conditions created by the extreme microscopic event.[7] Despite the unique advantages of CS, the deposition of glassy polymers can be particularly challenging because of their low fracture toughness[8] leading to μPs' fragmentation rather than yielding and adhesion. Therefore, understanding the polymer's fracture toughness and its nonlinear coupling with adiabatic shear-induced heating under ultrahigh-rate (UHR) deformation becomes crucial to realizing the solid-state consolidation of μPs not using any volatile organic compounds or additional heating.

In CS, μP adhesion is accomplished below the melting temperature or perhaps the glass transition temperature (T_g) of the μPs' constituent materials. However, certain limited regions of a colliding μP, e.g., near the contact interfaces with a substrate surface or other deposited μPs, can experience a rapid rise in temperature above the transition temperatures due to localized adiabatic plastic deformation and shear instability.[9] While the highly localized thermal softening (or melting) is crucial for the solid-state and solvent-free consolidation of μPs, other inelastic mechanisms, especially brittle fracture, may also become significant, even dominating plastic deformation. Under the fracture-dominant deformation, the kinetic energy of a μP is mainly dissipated by creating new surfaces. Consequently, this fracture-dominant inelastic deformation mode is disadvantageous in the aspect of localized thermal softening and eventually for deposition efficiency of CS. One may attempt to predict the UHR deformation

Received: April 18, 2022
Accepted: June 28, 2022
Published: July 11, 2022

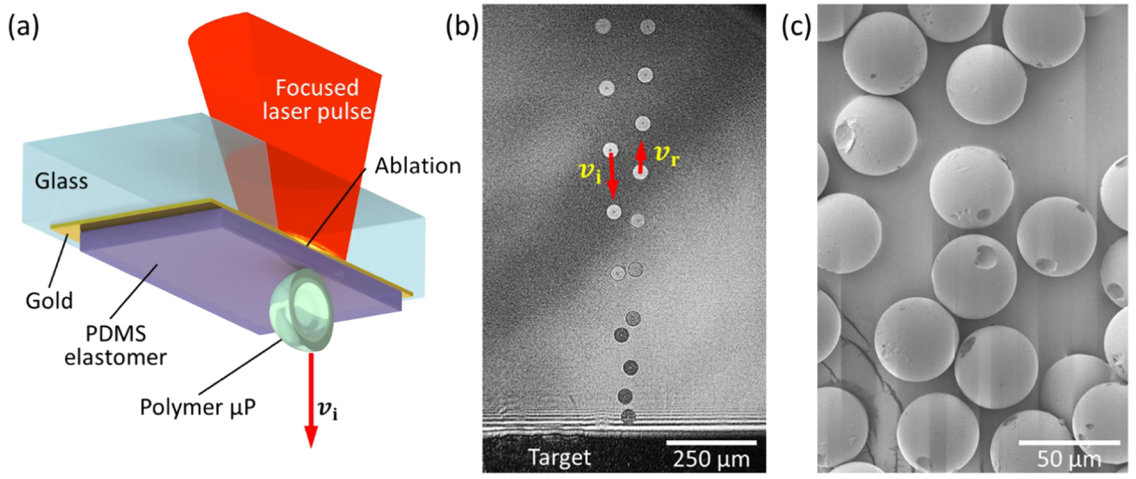

Figure 1. (a) Cross sectional illustration of the μP launching process in LIPIT. (b) Example of an ultrafast stroboscopic micrograph of a μP colliding with a PS substrate at v_i = 91 m/s. (c) Scanning electron microscopy (SEM) image of 100 kDa PS-μPs.

Table 1. Measured Glass Transition Temperatures of PS having Different M_n

M_n[a] (kDa)	PDI[a]	T_g	supplier
10	1.06	88.3 ± 1.1	Pressure chemical Co., Pittsburgh, PA
20	1.01	92.6 ± 0.5	Scientific polymer products Inc., Ontario, NY
40	1.04	97.3 ± 0.5	PSS GmbH, Mainz, Germany
100	1.04	96.4 ± 0.3	Scientific polymer products Inc., Ontario, NY

[a]PDIs and M_n are reported by the manufacturers.

characteristics of polymers through polymers' lower temperature deformation behavior according to the time−temperature superposition principle.[10] However, in the UHR inelastic deformation, local temperature fields, the consequence of impact-induced plastic strains, are coupled with temperature-dependent mechanical properties. Thus, the UHR adiabatic plasticity of polymers is inherently nonlinear and is very difficult to predict via the time−temperature superposition. More specifically, because the evolution of the physical state of μPs is nonlinearly governed by the interplay between the different inelastic processes, the experimental study of single μP UHR collisions can provide essential knowledge for the establishment of polymer-based CS additive manufacturing.

To address challenges from the complexity of the UHR deformation dynamics, the laser-induced projectile impact test (LIPIT)[11,12] has been introduced to produce single μP collisions (Figure 1) with precisely measured collision conditions, including the impact velocity (v_i) and rebound velocity (v_r) of individual μPs with a known diameter (D_p) and mass (m_p). Since the first use of LIPIT in the characterization of single-crystal silver μPs,[13] LIPIT has been widely used for various single μP characterizations. The increasing use of LIPIT is attributed to the capabilities of the method providing a proper range of v_i for typical D_p of CS feedstock powders.[14] For example, the spectra of v_r for polystyrene (PS) and polyimide μPs were measured as a function of v_i for basic knowledge of the actual CS deposition yield.[15] The LIPIT study of core−shell μPs containing thermoset epoxy resin was performed for the fractographical study of the μPs.[16,17] In addition to the kinematic measurements and post-impact characterizations, dynamic frictional coefficients of PS and PS-contained block copolymer μPs were quantified using angled LIPIT when they collided with rigid substrates at an impact angle of 45°.[6] This angled LIPIT study demonstrated that nonlinear interfacial rheological properties could be quantified in terms of the frictional coefficients. However, despite the success of LIPIT-based studies, the characteristic effects of the molecular weights of polymers on the consolidation process have not yet been fully or deliberately explored. Herein, the unique interplay between plastic yielding and fracture as functions of molecular weight is discussed with PS as a model glassy polymer.

MATERIALS AND METHODS

Synthesis of μPs. Monodispersed PS-μPs were produced from purchased PS powders using the methods of Bacha et al.[18] Solutions of PS (each having a different number-averaged molecular weight, M_n) at 5% w/v were prepared with narrow polydispersity indices (PDIs) and dispersed in microfluidic devices with aqueous 2% w/v 72 kDa polyvinyl alcohol (87.0−89.0% hydrolyzed, MP Biomedicals). Droplets were left as suspensions in an open beaker overnight to allow for solvent evaporation. PS-μPs were transferred to a round-bottom flask and stirred with a paddle stirrer at 60 °C for 6 h. The flask was left to cool overnight and then filtered through a 45 μm sieve to remove large particles and contaminants. The particles were washed with deionized water, isopropanol, and hexanes before being transferred to a vacuum chamber to dry. Samples were dried for 14 days at 70 °C under a vacuum (Figure 1c). T_g was determined by differential scanning calorimetry (DSC) in triplicate. Samples of 5−10 mg were prepared in Tzero hermetically sealed pans and heated under nitrogen twice from 0 to 150 °C in a TA Instruments Discovery DSC 2500. T_g was determined from the second heating cycle. Details regarding molecular weight, PDI, and T_g of the utilized PS are listed in Table 1. Note that noticeable aging effects were observed from DSC curves (Figure S1) in the preparation of the PS specimens. As the aging effects were inevitable, each set of

https://doi.org/10.1021/acsomega.2c02419
ACS Omega 2022, 7, 26465−26472

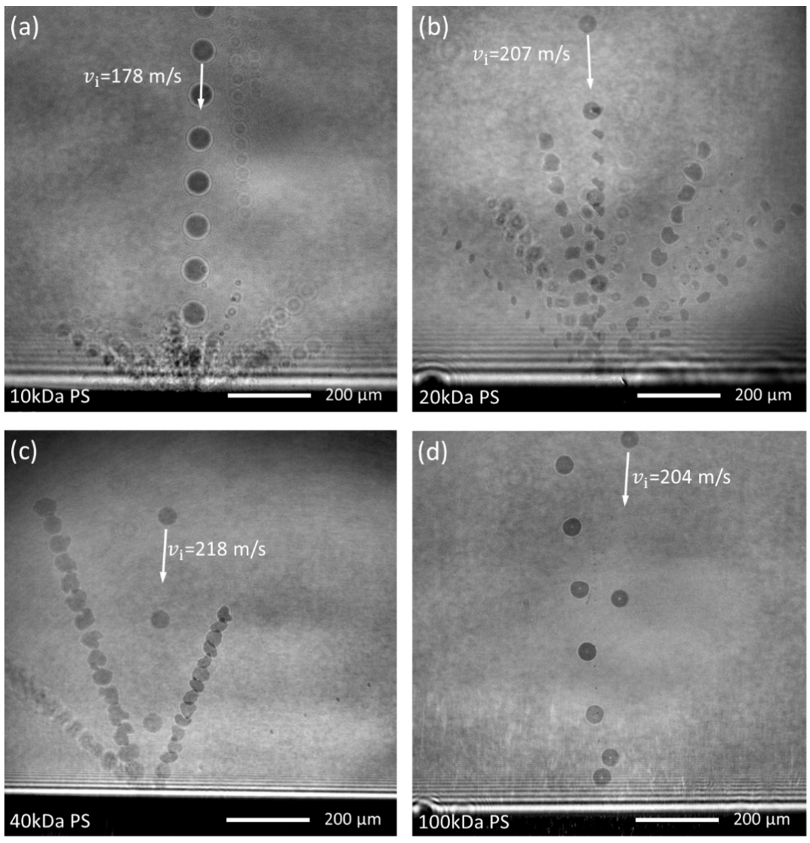

Figure 2. Examples of ultrafast stroboscopic micrographs of (a) 10 kDa, (b) 20 kDa, (c) 40 kDa, and (d) 100 kDa PS-μPs colliding with the PS substrates at impact velocities of approximately 200 m/s.

PS-μPs and PS substrates with varying M_n were equally treated not to influence the main findings in this study.

Conditions for the Microscopic Collision Experiment. The LIPIT technique was used to individually accelerate PS-μPs placed on a launchpad to speeds ranging from 50 to 950 m/s. The launchpads were prepared by spin coating thermally curable poly(dimethylsiloxane) (PDMS; Sylgard 184, Corning) on an 80 nm thick gold coated cover glass (FisherBrand) at 1000 RPM for 30 s and subsequently cured at 120 °C for 2 h. A 1,064 nm laser pulse (Spectra-Physics INDI-10) was used to ablate the gold layer below a targeted μP. Local laser ablation of the gold layer beneath the target μP creates a rapid expansion of the elastomer film, indirectly accelerating the μP without exposure to the high-temperature ablation event (Figure 1a). The resultant collisional motion of the accelerated μP was captured by a stroboscopic imaging technique utilizing evenly gated ultrafast (<1 ps) white light pulses (Figure 1b). In PS-on-PS experiments, PS-μPs of varying number-averaged molecular weights (M_n = 10, 20, 40, and 100 kDa) were impacted on PS target substrates (~5 mm × 5 mm) of the same M_n to systematically study the effect of M_n on the impact dynamics. Information on how the mechanical properties of monodisperse molecular weight polystyrenes change with varying molecular weight can be found elsewhere.[19,20] The detailed procedure for preparing the PS substrates is described in the Supporting Information. The PS target substrates' thickness was at least 10 times greater than the diameter of impacting PS-μPs. Due to the short impact time, these experiments were assumed to represent a semi-infinite substrate condition. In PS-on-Si experiments, the PS-μPs of varying M_n were impacted on a silicon (Si) substrate to observe the effects of substrate rigidity. Because roughness values of PS and Si substrates were 1.65 and 0.55 nm, respectively (Figure S2), they were considered smooth surfaces in this study. Additionally, while the PS target substrates showed the typical chemistry of PS in terms of the water wetting angle, the wetting angle of the Si substrate was close to that of the silica substrate due to its native oxide (Figure S3).

RESULTS AND DISCUSSION

Deformation Images of μP Collisions. The collision characteristics of PS-μPs were investigated by ultrafast stroboscopy for their M_n-dependent UHR behaviors. Due to the glassy nature of PS, most PS-μPs were shattered after collision with the PS substrates for $M_n \leq 40$ kDa, at increased v_i (Figure 2). Note that the shattered collision was defined when fragmentation of PS-μPs was visually identified in the stroboscopic image. Fewer fragments were consistently produced from higher M_n PS-μPs, while none of the 100 kDa PS-μPs experienced shattering. Moreover, the 10 kDa PS-μPs were fractured even in the launching process (preimpact fracture) when they were subjected to higher acceleration to reach v_i > 200 m/s. The observed characteristics were understood by the positive correlation of fracture toughness with M_n[21] that were consistent with our previous microballistic perforation study of freestanding PS films.[22] The entanglement density of PS, given by $(1 - M_c/M_n)2N_0\rho/3M_c$,[23] linearly increased the energy required to perforate the PS films, where N_0, ρ, and M_c are Avogadro's number, the mass density, and a critical molecular weight (~31 kDa) of PS, respectively. With respect to solvent-free (solid-state) coating, the brittle nature

https://doi.org/10.1021/acsomega.2c02419
ACS Omega 2022, 7, 26465−26472

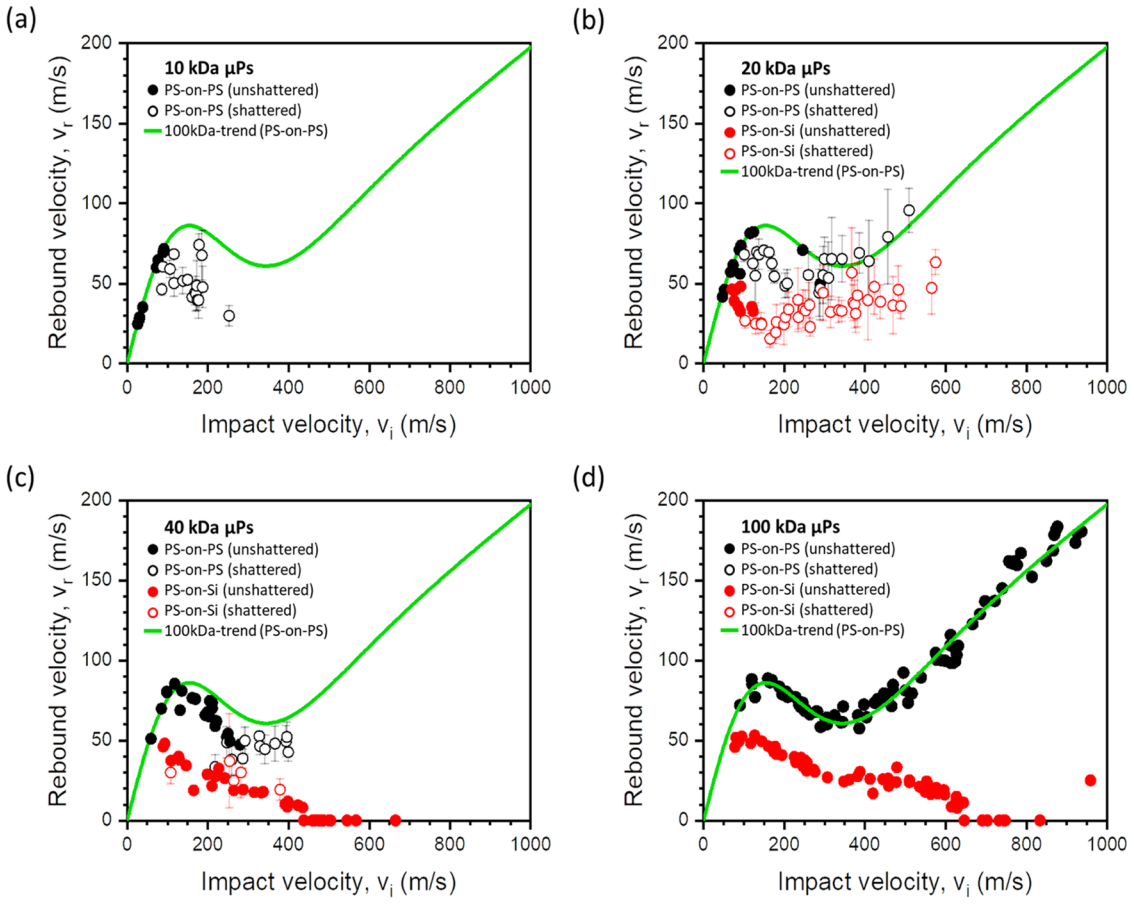

Figure 3. v_r-spectra of PS-μPs in collision with PS and Si substrates. (a) M_n = 10 kDa, (b) M_n = 20 kDa, (c) M_n = 40 kDa, and (d) M_n = 100 kDa for both μPs and the substrate. The trend of PS-on-PS results of M_n = 100 kDa (green curve) is co-plotted for reference. The scatter bar of each shattered event indicates the standard deviation of rebound velocities of identifiable shattered fragments.

of glassy polymers, including PS, is undoubtedly one of the most critical challenges to be addressed, as discussed earlier.

Rebound and Adhesion Characteristics of μPs. The v_r-spectra of the PS-μPs were measured until the fracture trends were consistent (Figure 3). For shattered collisions, the mean value of v_rs of analyzable shattered fragments was used with a scatter bar representing the standard deviation of the fragments' v_r. Due to the lack of shattering, the v_r-spectra of 100 kDa μPs in PS-on-PS provide a useful reference trend (the green curves in Figure 3) to compare characteristics of the other M_n μPs through the entire range of v_i. The green curve was from the fitting of the coefficients of restitution (CoR), which will be discussed in detail later. Regardless of M_n, unshattered μPs showed nearly the same v_r behavior in PS-on-PS. However, the shattered events demonstrated considerably lower v_r, and this observation strongly indicated a fracture-driven energy dissipation mechanism. Moreover, although v_r typically increases with v_i, an inverse trend was observed in a range from 200 to 350 m/s. This unusual inverse trend is because the μPs underwent exponentially growing inelastic processes such as fracture and softening within this range. In Figure 3b, two unshattered events were within a range of the shattering events of PS-on-PS. These outliers could be originating from the instability of the fracture-dominant deformation process or some unidentified defects of the PS-μPs or the PS substrate. Interestingly, the 100 kDa μPs did not show adhesion to the PS substrate over the entire range of v_i although the substantially entangled PS completely suppressed the shattering process. As the PS-on-PS can be analogous to a thick coating condition in CS, the lack of adhesion events indicates that the continuous deposition of PS feedstock powder could be challenging. Interestingly, when changing the deformable PS substrate to a rigid silicon substrate (PS-on-Si), the v_r-spectra of the PS-μPs were drastically altered. First, the reduction of v_r is universal regardless of M_n. Second, the PS-μPs demonstrated substantially less shattering (Figure 3c), a counterintuitive result since one may expect that collisions with more rigid substrates would cause more severe shattering. This observation implies that fracture and plastic yielding compete during impact-induced deformation and that more thermal softening occurs within PS-μPs during impact with the silicon substrate. This hypothesis will be verified through post-collision characteristics and numerical modeling in a later section. Third, both 40 and 100 kDa μPs demonstrated adhesion to the Si substrate. The onset velocities of adhesion, or the critical velocities (v_c), for the 40 and 100 kDa μPs were approximately 435 m/s (Figure 3c) and 645 m/s (Figure 3d), respectively.

CoR Spectra and Fitting. The nonmonotonic trend of the v_r-spectra implies the complexity of the UHR collision dynamics that may be originating from multiple mechanisms. In this aspect, the dimensionless spectra of CoR ($=v_r/v_i$) can be helpful for the material's nonlinear responses as simple elastic responses are normalized (Figure 4). For example, the peak near 200 m/s in the v_r-spectrum (Figure 3d) did not appear in the CoR-spectrum (Figure 4d). Despite the simpler

https://doi.org/10.1021/acsomega.2c02419
ACS Omega 2022, 7, 26465−26472

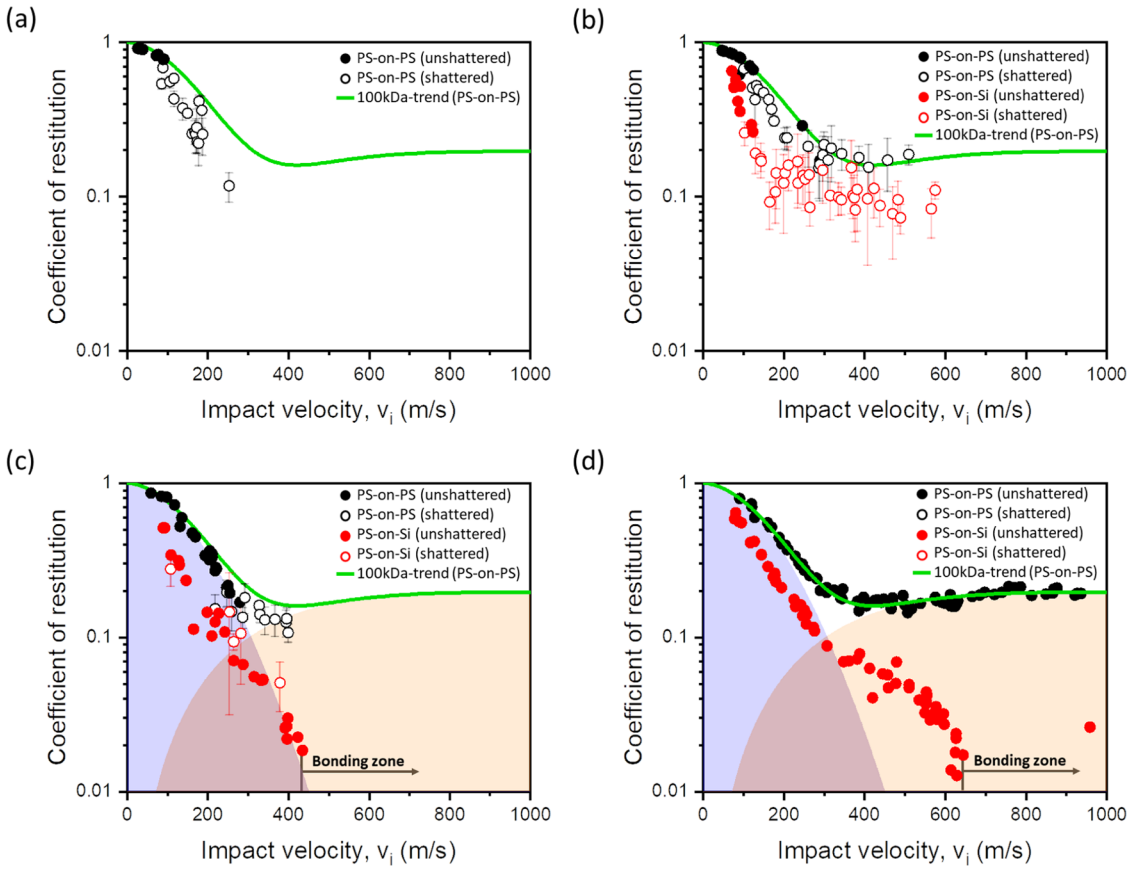

Figure 4. CoR spectra of PS-μPs in collision with PS and Si substrates for (a) M_n = 10 kDa, (b) M_n = 20 kDa, (c) M_n = 40 kDa, and (d) M_n = 100 kDa. The scatter bar of each shattered event indicates the standard deviation of CoR values of identifiable shattered fragments. The fitting curve for 100 kDa (green) is co-plotted in all other plots for reference. The blue and orange shaded regions, corresponding to the two terms of the fitting curve, f_{ep} (blue) and f_{es} (orange), are also displayed in (c) and (d).

trend, the CoR-spectrum of 100 kDa PS-on-PS still exhibited a nonmonotonic trend with a minimum near 430 m/s. The whole collision process consists of an impact stage (deceleration of the center-of-mass), subsequently followed by a rebound stage (reverse acceleration of the center-of-mass), requiring that the center-of-mass pauses between the two stages. Therefore, the kinetic energy associated with the rebound motion can be decomposed into the respective elastic recoiling contributions of the μP and the substrate when bonding between the μP and the substrate was insignificant (more reasonable for the low-v_i regime). Based on this understanding, we hypothesized that the CoR-spectrum of 100 kDa PS-on-PS was produced by two elastic recoiling contributions primarily from the μP and the substrate, f_{ep} and f_{es}. Thus, two exponential functions were phenomenologically introduced for the respective contributions, as shown in eq 1.

$$\mathrm{CoR}(v_i) \cong f_{ep} + f_{es} = e^{-(v_i/v_p)^m} + \alpha_s[1 - e^{-(v_i/v_s)^m}] \quad (1)$$

The respective fitting parameters, v_p, v_s, α_s, and m, were identified as 195.2 ± 1.6 m/s, 367.6 ± 19.5 m/s, 0.20 ± 0.004, and 1.82 ± 0.04, respectively, for the 100 kDa PS-on-PS spectrum of CoR. Since the exponent, m, is close to 2, the overall trend is dominantly driven by the kinetic energy in μP. At the high end of v_i, CoR tends to be saturated to α_s~0.2, meaning that the recoiling behavior of the PS substrate remained the same within this COR plateau. In other words, the PS substrate did not undergo substantial softening or melting up to 1000 m/s. Note that this fitted curve was also used to show the trend of $v_r = v_i$ CoR in Figure 3. In this model, while f_{ep} mainly represents exponentially decaying residual elasticity of the μP, f_{es} represents an increasing elastic contribution of the PS substrate. As v_i increases, f_{ep} is rapidly reduced through the inelastic mechanisms, i.e., fracture and visco-plastic yielding, within a single μP. In contrast, the trend of f_{es} indicated that the semi-infinite PS substrate did not undergo an inelastic deformation as severely as the μP. Thus, the substrate supports a higher recoiling response for higher v_i. The comparably smaller inelastic deformation of the PS substrate compared with that of the μP is shown in Figure S6 by comparing the plastic strain fields developed in the two bodies.

According to the CoR spectra of PS-on-Si, more inelastic deformation via fracturing and yielding was evident regardless of M_n, due to the substantially larger elastic modulus of silicon (~170 GPa)[24] than PS (~3.5 GPa).[25] The considerably larger v_c of 100 kDa μPs compared to 40 kDa μPs meant that double the kinetic energy of the μP was required to create the bonding state. This additionally required energy for 100 kDa μPs was related to the difference in the CoR trends prior to the bonding zone. The CoR trend of 40 kDa PS-on-Si was exponentially reduced without a considerable recoiling contribution from the Si substrate (Figure 4c). However, the CoR trend of 100 kDa PS-on-Si exhibited a sizable recoiling contribution (apparent for v_i = 400−600 m/s) from the Si

https://doi.org/10.1021/acsomega.2c02419
ACS Omega 2022, 7, 26465−26472

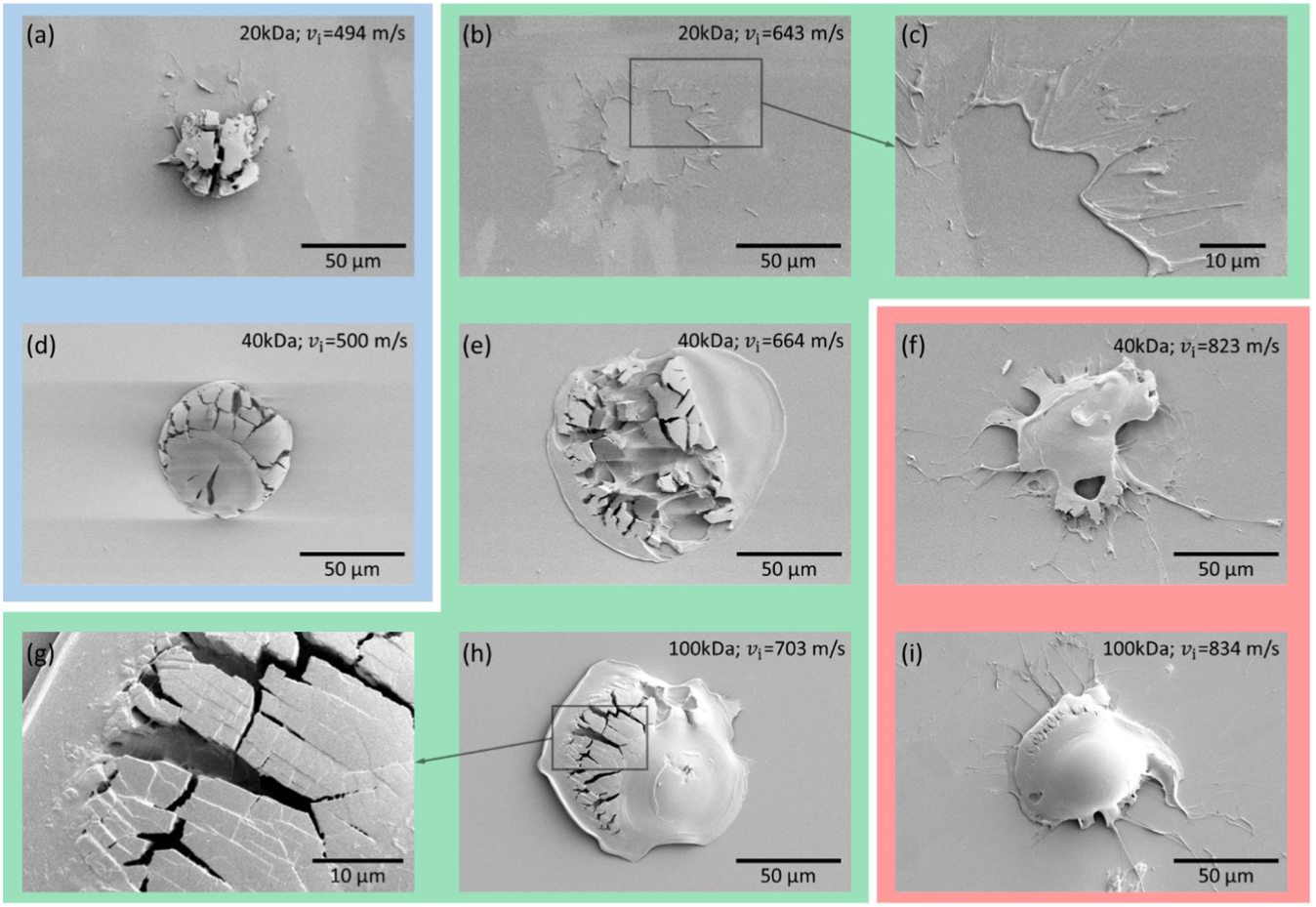

Figure 5. SEM images of PS-μPs after colliding with the Si substrate at different velocities: (a)−(c) M_n = 20 kDa, (d)−(f) M_n = 40 kDa, and (g)−(i) M_n = 100 kDa. Three v_i-ranges around 500 m/s, 650 m/s, and 830 m/s are displayed in blue, green, and red panels, respectively.

substrate even though this contribution was relatively weaker than that of the PS substrate (Figure 4d). The substrate's elastic recoiling tends to hinder the bonding state. In other words, the absence of the substrate's elastic contribution in the 40 kDa PS-on-Si implies that interfacial adhesion of μPs to the Si substrate was large enough to suppress the elastic recoiling of the Si substrate. The origin of this enhanced adhesion contribution in the 40 kDa PS-on-Si will be discussed later.

Characteristic Features of Bonded μPs. The μPs adhered to a Si substrate were assessed using scanning electron microscopy (SEM) to understand the dynamic characteristics of μPs. Adhered μPs at three v_i-ranges around 500, 650, and 830 m/s are displayed in Figure 5. In the 500 m/s range, although the 20 kDa μP was shattered, it still left some partially bonded fragments and a minor residue from jetting on the Si substrate (Figure 5a). However, despite its complete fracture, the 40 kDa μP did not experience any meaningful mass loss (Figure 5d). Moreover, no evident sign of jetting was shown. Meanwhile, 100 kDa μPs were not left on the substrate in this v_i-range. In the 650 m/s range, the 20 kDa μP was completely shattered without any residual fragments (Figure 5b), but an annular remnant of jetting was observed (Figure 5c). In contrast, the 40 kDa μP showed brittle fragments bonded by a plastically deformed material without jetting remnants (Figure 5e). The suppression of jetting may primarily be due to the higher dynamic viscosity of 40 kDa PS in its melt state than that of 20 kDa PS. The 100 kDa μP also demonstrated the co-existence of fragments and plastically deformed materials without jetting remnants (Figure 5h) with a relatively lower volume portion of fragments. The fractured region revealed exceptionally fine fragments and fibrils with craze produced by biaxial strains (Figure 5g). The delaminated and contracted perimeter of the bonded 100 kDa μP, not seen from the 40 kDa μP, clearly indicated the decreased adhesion to the substrate. This observation is also consistent with the previous discussion based on the contrasting trends of the CoR spectra appearing for v_i = 400−600 m/s, prior to the bonding zone (Figure 4c,d). In other words, as the PS melt of 40 kDa was less viscous than that of 100 kDa, the 40 kDa PS provided better wetting on the Si substrate. Note that the dynamic viscosity of PS melts at a constant temperature is known to be insensitive to M_n at high-strain rate cyclic loading conditions.[26] However, we still believe that the M_n-dependent adhesion behavior is originating from the localized thermo-rheological difference of PS melts. In the collision-induced deformation, because the shear deformation of a μP and its temperature are under positive feedback, a condition known as adiabatic shear instability,[27] the resultant rheological effect of M_n can be amplified to produce a more pronounced difference in wetting. In the 830 m/s range, both 40 and 100 kDa showed a significant mass loss and prominent jetting features (Figure 5f,i). As a result, the corresponding deposition efficiency is reduced. Note that the rheological effects of polymer melts in CS are more important than the conventional CS for metals because viscosities of molten metals[28] are several orders lower than those of polymers.

https://doi.org/10.1021/acsomega.2c02419
ACS Omega 2022, 7, 26465−26472

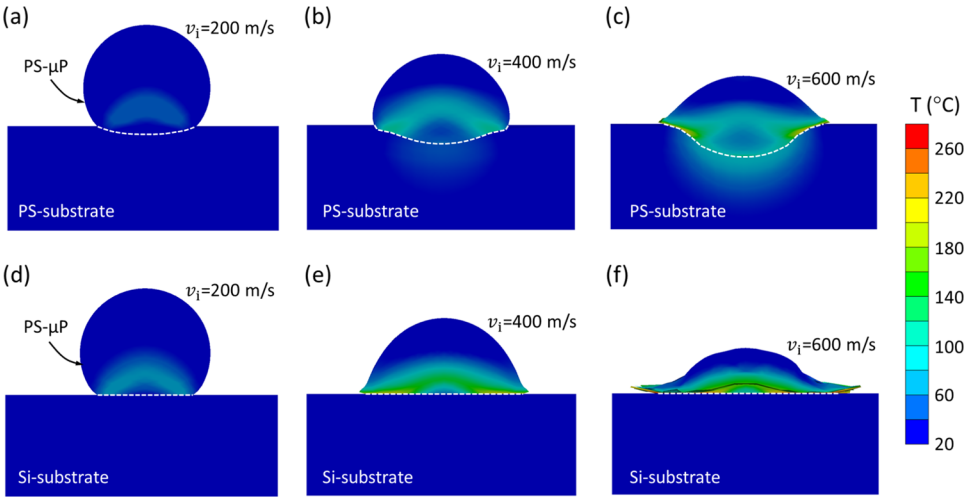

Figure 6. Temperature profiles obtained from FEA simulations of (a)−(c) PS-on-PS and (d)−(f) PS-on-Si impact for M_n = 100 kDa at v_i = 200, 400, and 600 m/s. Contour maps show the deformed μPs when the velocity of their center-of-mass is zero. Horizontal dashed lines represent the location of the interface.

The effect of collision-induced plastic deformation and the resultant temperature rise in the μPs with regard to substrate stiffness (i.e., PS versus Si substrate) was further examined through finite element analysis (FEA) simulations of the impact process (see the Supporting Information for more details). As shown in Figure 6, 100 kDa PS-μPs' impact on the stiffer substrate was significantly more likely to increase the temperature of the μP beyond its T_g. This increase in the overall temperature of the impacted μP was attributed to the higher dissipation of the kinetic energy through plastic deformation. Moreover, localized high-temperature regions over 200 °C, far beyond T_g, were predicted at the contact interface in the PS-on-Si case. This favorable condition for interfacial melting supports a higher adhesion probability for the PS-on-Si case.

CONCLUSIONS

For the solvent-free and solid-state deposition of glassy polymers, the M_n-dependent interplay of the primary inelastic mechanisms is systematically and comprehensively investigated through ultrafast optical images from LIPIT, v_r- and CoR spectra, SEM images, and FEA numerical modeling. Regardless of M_n, the solid-state deposition of PS-μPs on a PS substrate seems to be challenging. For low-M_n PS below its critical entanglement density, μPs are shattered upon collision with the PS substrate since the fracture process dominates over the yield process in the collision-induced deformation. Although the severe brittle fragmentation can be circumvented by increasing M_n of μPs, the deformable PS substrate hampers the adhesion of μPs by causing insufficient thermal softening of μP and recoiling to μP. Interestingly, the solid-state deposition of PS μPs is feasible for a Si substrate, which is substantially more rigid than PS. While the fracture process is hindered by entangled large molecules ($M_n \geq 40$ kDa), sufficient adiabatic shear-induced thermal softening can overwhelm fracture response because of the increased shear rates during the collision with the rigid substrate. This observation suggests that the two competing processes of fracture and plastic yielding are under a dynamic balance determined by deformation rates. Moreover, although the high M_n can bring a positive effect on the adhesion process by reducing the brittle fracture mode of μPs, an excessively high M_n can result in weak adhesion. In the presence of the adiabatic shear instability, we believe that the dynamic viscosity of melt PS formed at the adhesion interface can result in insufficient wetting behavior due to the overly viscous PS melts for excessively high M_n. Due to the opposite effects of M_n on deformation and adhesion via fracture toughness ($T < T_g$) and dynamic viscosity ($T > T_g$), our study demonstrates that the proper selection of M_n is crucial for the feasibility of the solvent-free and solid-state deposition of glassy polymers. Moreover, this complicated M_n-dependent rheological behavior has not been an issue in the traditional CS using metal μPs as the interfacial viscosity of metals abruptly drops near their melting temperatures. Therefore, we believe that more extensive UHR studies should be followed to establish the polymer-based CS with more designed polymer systems having tailored distributions of M_n and functional additives.

ASSOCIATED CONTENT

Supporting Information

The Supporting Information is available free of charge at https://pubs.acs.org/doi/10.1021/acsomega.2c02419.

Aging characteristics of polystyrene microparticles and substrates; surface roughness and chemistry of target substrates; finite element model and boundary conditions; material constitutive model; finite element model validation (PDF)

AUTHOR INFORMATION

Corresponding Author

Jae-Hwang Lee − *Department of Mechanical and Industrial Engineering, University of Massachusetts, Amherst, Massachusetts 01003, United States;* orcid.org/0000-0002-2546-1044; Email: leejh@umass.edu

Authors

Anuraag Gangineri Padmanaban − *Department of Mechanical and Industrial Engineering, University of Massachusetts, Amherst, Massachusetts 01003, United States;* orcid.org/0000-0002-0684-9799

https://doi.org/10.1021/acsomega.2c02419
ACS Omega 2022, 7, 26465−26472

Tristan W. Bacha − *Department of Chemical Engineering, Rowan University, Glassboro, New Jersey 08028, United States*

Jeeva Muthulingam − *Department of Mechanical Engineering, Rowan University, Glassboro, New Jersey 08028, United States*

Francis M. Haas − *Department of Mechanical Engineering, Rowan University, Glassboro, New Jersey 08028, United States;* orcid.org/0000-0001-7511-0392

Joseph F. Stanzione, III − *Department of Chemical Engineering, Rowan University, Glassboro, New Jersey 08028, United States;* orcid.org/0000-0003-0464-835X

Behrad Koohbor − *Department of Mechanical Engineering, Rowan University, Glassboro, New Jersey 08028, United States;* orcid.org/0000-0002-5787-4644

Complete contact information is available at: https://pubs.acs.org/10.1021/acsomega.2c02419

Notes

The authors declare no competing financial interest.

■ ACKNOWLEDGMENTS

This research was sponsored by the U.S. DEVCOM Army Research Laboratory under Cooperative Agreement No. W911NF-19-2-0152.

■ REFERENCES

(1) Raoelison, R. N.; Xie, Y.; Sapanathan, T.; Planche, M. P.; Kromer, R.; Costil, S.; Langlade, C. Cold Gas Dynamic Spray Technology: A Comprehensive Review of Processing Conditions for Various Technological Developments till to Date. *Addit. Manuf.* **2018**, 134−159.

(2) Assadi, H.; Kreye, H.; Gärtner, F.; Klassen, T. Cold Spraying − A Materials Perspective. *Acta Mater.* **2016**, *116*, 382−407.

(3) Xu, Y.; Hutchings, I. M. Cold Spray Deposition of Thermoplastic Powder. *Surf. Coat. Technol.* **2006**, *201*, 3044−3050.

(4) Moridi, A.; Hassani-Gangaraj, S. M.; Guagliano, M.; Dao, M. Cold Spray Coating: Review of Material Systems and Future Perspectives. *Surf. Eng.* **2014**, *30*, 369−395.

(5) Li, L.; de Jeu, W. H. Shear-Induced Smectic Ordering in the Melt of Isotactic Polypropylene. *Phys. Rev. Lett.* **2004**, *92*, No. 075506.

(6) Kim, A.; Müftü, S.; Thomas, E. L.; Lee, J.-H. Extreme Tribological Characteristics of Copolymers Induced by Dynamic Rheological Instability. *ACS Appl. Polym. Mater.* **2021**, *3*, 4413−4418.

(7) Schwager, T.; Pöschel, T. Coefficient of Restitution for Viscoelastic Spheres: The Effect of Delayed Recovery. *Phys. Rev. E* **2008**, *78*, No. 051304.

(8) Kim, B. H.; Joe, C. R.; Otterson, D. M. On the Determination of Fracture Toughness in Polymers. *Polym. Test.* **1988**, *8*, 119−130.

(9) Xie, W.; Alizadeh-Dehkharghani, A.; Chen, Q.; Champagne, V. K.; Wang, X.; Nardi, A. T.; Kooi, S.; Müftü, S.; Lee, J.-H. Dynamics and Extreme Plasticity of Metallic Microparticles in Supersonic Collisions. *Sci. Rep.* **2017**, *7*, No. 5073.

(10) Menczel, J. D.; Prime, R. B. *Thermal Analysis of Polymers*; Menczel, J. D.; Prime, R. B., Eds.; John Wiley & Sons, Inc.: Hoboken, NJ, USA, 2009. DOI: 10.1002/9780470423837.

(11) Lee, J.-H.; Wang, L.; Boyce, M. C.; Thomas, E. L. Periodic Bicontinuous Composites for High Specific Energy Absorption. *Nano Lett.* **2012**, *12*, 4392−4396.

(12) Lee, J.-H.; Loya, P. E.; Lou, J.; Thomas, E. L. Dynamic Mechanical Behavior of Multilayer Graphene via Supersonic Projectile Penetration. *Science* **2014**, *346*, 1092−1096.

(13) Thevamaran, R.; Lawal, O.; Yazdi, S.; Jeon, S.-J. J.; Lee, J.-H.; Thomas, E. L. Dynamic Creation and Evolution of Gradient Nanostructure in Single-Crystal Metallic Microcubes. *Science* **2016**, *354*, 312−316.

(14) Veysset, D.; Lee, J.-H.; Hassani, M.; Kooi, S. E.; Thomas, E. L.; Nelson, K. A. High-Velocity Micro-Projectile Impact Testing. *Appl. Phys. Rev.* **2021**, *8*, No. 011319.

(15) Khalkhali, Z.; Xie, W.; Champagne, V. K.; Lee, J.-H.; Rothstein, J. P. A Comparison of Cold Spray Technique to Single Particle Micro-Ballistic Impacts for the Deposition of Polymer Particles on Polymer Substrates. *Surf. Coat. Technol.* **2018**, *351*, 99−107.

(16) Yang, G.; Xie, W.; Huang, M.; Champagne, V. K.; Lee, J.-H.; Klier, J.; Schiffman, J. D. Polymer Particles with a Low Glass Transition Temperature Containing Thermoset Resin Enable Powder Coatings at Room Temperature. *Ind. Eng. Chem. Res.* **2019**, *58*, 908−916.

(17) Huang, M.; Liu, Y.; Khalkhali, Z.; Kim, A.; Hu, W.; Lee, J. H.; Rothstein, J. P.; Klier, J.; Schiffman, J. D. Epoxy Resin-Encapsulated Polymer Microparticles for Room-Temperature Cold Sprayable Coatings. *ACS Appl. Mater. Interfaces* **2021**, *13*, 50358−50367.

(18) Bacha, T. W.; Manuguerra, D. C.; Marano, R. A.; Stanzione, J. F. Hydrophilic Modification of SLA 3D Printed Droplet Generators by Photochemical Grafting. *RSC Adv.* **2021**, *11*, No. 21745.

(19) McCormick, H. W.; Brower, F. M.; Kin, L. The Effect of Molecular Weight Distribution on the Physical Properties of Polystyrene. *J. Polym. Sci.* **1959**, *39*, 87−100.

(20) Wool, R. P.; Yuan, B. -L.; McGarel, O. J. Welding of Polymer Interfaces. *Polym. Eng. Sci.* **1989**, *29*, 1340−1367.

(21) Hui, C. Y.; Kramer, E. J. Molecular Weight Dependence of the Fracture Toughness of Glassy Polymers Arising from Crack Propagation through a Craze. *Polym. Eng. Sci.* **1995**, *35*, 419−425.

(22) Xie, W.; Lee, J.-H. Dynamics of Entangled Networks in Ultrafast Perforation of Polystyrene Nanomembranes. *Macromolecules* **2020**, *53*, 1701−1705.

(23) Bersted, B. H. Entanglement Network Model Relating Tensile Impact Strength and the Ductile-brittle Transition to Molecular Structure in Amorphous Polymers. *J. Appl. Polym. Sci.* **1979**, *24*, 37−50.

(24) Wortman, J. J.; Evans, R. A. Young's Modulus, Shear Modulus, and Poisson's Ratio in Silicon and Germanium. *J. Appl. Phys.* **1965**, *36*, 153−156.

(25) Miyake, K.; Satomi, N.; Sasaki, S. Elastic Modulus of Polystyrene Film from near Surface to Bulk Measured by Nano-indentation Using Atomic Force Microscopy. *Appl. Phys. Lett.* **2006**, *89*, No. 31925.

(26) Onogi, S.; Kato, H.; Ueki, S.; Ibaragi, T. Rheological Properties of Polystyrene Melts. *J. Polym. Sci., Part C: Polym. Symp.* **2007**, *15*, 481−494.

(27) Grujicic, M.; Zhao, C.; DeRosset, W.; Helfritch, D. Adiabatic Shear Instability Based Mechanism for Particles/Substrate Bonding in the Cold-Gas Dynamic-Spray Process. *Mater. Des.* **2004**, *25*, 681−688.

(28) Dinsdale, A. T.; Quested, P. N. The Viscosity of Aluminium and Its Alloys—A Review of Data and Models. *J. Mater. Sci.* **2004**, *39*, 7221−7228.